SPIN
Vol. 7, No. 1 (2017) 1740007 (12 pages)

DOI: 10.1142/S2010324717400070

Spin-Transfer-Torque Driven Vortex Dynamics in Electrodeposited Nanowire Spin-Valves

Flavio Abreu Araujo
Unité Mixte de Physique CNRS, Thales
Univ. Paris-Sud, Université Paris-Saclay
Palaiseau F91767, France
flavio.abreuaraujo@cnrs-thales.fr

Luc Piraux*
Institute of Condensed Matter and Nanosciences
Université catholique de Louvain, Louvain-la-Neuve
BE-1348, Belgium
luc.piraux@uclouvain.be

Received 3 February 2017
Accepted 27 April 2017
Published 25 May 2017

A bottom-up approach for the fabrication of an assembly of electrodeposited nanowires has been combined to single nanowire electrical connection techniques to investigate the spin-transfer-torque and microwave emission of specially designed nanowires containing Co/Cu/Co pseudo spin-valves (SVs). Porous alumina templates are used for the growth by electrodeposition of metallic in-series connected SVs. Under specific magnetic field and injected current conditions, emission of microwave current is detected with frequency in the GHz range and linewidth as low as 1.8 MHz. Microwave signals have been obtained even at zero magnetic field and high frequency versus magnetic field tunability was demonstrated. Our findings are in good agreement with micromagnetic simulations. In addition, it appears that in our particular geometry, the microwave emission is generated by the vortex gyrotropic motion which occurs in, at least, one of the two magnetic layers of our SV structures.

Keywords: Nanowire; spin-valve; spin-torque oscillator; spin-transfer-torque; magnetic vortex.

1. Introduction

It has been shown[1–4] that the spin-transfer-torque (STT) effect predicted by Slonczewski[5] and Berger[6] can be used to overcome the Gilbert damping in such a way that it is possible to obtain coherent magnetization oscillation in magnetic spin-valve (SV) nanostructures. In these conditions, the nanoscale SVs under study became the so-called spin-torque nano-oscillators (STNO) that have been the subject of intensive experimental and theoretical investigations during the last decade.

Theoretical and experimental studies have reported the strong influence of the nonlinear character of the microwave properties of STNOs, namely spectral coherence,[7,8] tunability,[9] frequency modulation,[10,11] or ability to synchronize to an external signal.[12,13]

*Corresponding author.

Initially,[2–4] the STNOs used single-domain-like magnetization distribution for the free magnetic layer of the SV. Recently,[14–30] focus has been directed to another very promising and naturally stable magnetization distribution in nano-scale magnetic layers with adequate aspect ratio: the magnetic vortex state.

Contrary to uniformly magnetized STNOs, it has been highlighted that the vortex case (STVOs) has the ability to conserve large frequency tunability with current through the Oersted field influence.[15]

The vortex state constitutes one of the possible ground magnetic states of soft ferromagnetic submicrometer elements. Such a topological magnetization distribution originates from the interplay between the magneto-static and exchange energy and is characterized by an in-plane closed flux domain structure with a vortex core at the center where the magnetization turns out of plane to minimize the high energetic configuration of anti-aligned moments.

For suitable current and magnetic field conditions and even without[15,17,22,23,27] any magnetic field, the vortex state can be excited by the injection of a dc current through a SV stack. The vortex dynamical excitation of interest is the gyrotropic motion of the vortex core driven by the spin-transfer-torque effect. Using both the gyrotropic vortex motion and the giant magnetoresistance (GMR) or tunnel magnetoresistance (TMR) electrical measurements, it was possible to obtain more coherent[15,22] and larger power output[17,22,31] microwave signals than previously with uniform mode oscillations.

When vortex-based spin-torque oscillators are considered, zero field emission can be achieved by using a special configuration of the vortex magnetic states. Indeed, it happens when each magnetic layer of the SV contains one vortex and their polarities are opposite as predicted by micromagnetic simulations and measured in electrodeposited spin-valves[23,27] and in lithographed nanopillars.[22]

However, these microwave emission linewidth and output power must still be improved in order to reach the values required for the targeted telecommunication applications. A commonly believed solution to overcome this issue is to synchronize several STNOs as it is expected to increase the generated microwave power.[32] Although coherent emission of a small number has been observed in a few studies involving a parallel connection of STNOs,[17,24,26,33] the extension of such synchronization to large arrays of STNOs implies both fundamental[34] as well as important technical challenges. Also, a series connection of STNOs[32,35–37] is very desirable, which is difficult to achieve using standard lithographically defined STNOs because of the relatively large aspect ratio that is required. This last issue may be tackled using a bottom-up template-based approach for the fabrication of STNOs.[23,27,38,39] By successive electrodeposition of metallic SVs into the pores of anodized aluminum oxide (AAO) template, each of them being separated by a nonmagnetic spacer, STNO stacks connected in series can be obtained. This technique has a real potential to fabricate, in an extremely cheap, fast and easy way, a dense array of long nanowires.

Beyond its complementary metal-oxide semiconductor (CMOS) compatibility, excellent thermal and mechanical properties, tunable pore diameter and inter-pore distance, AAO templates supported on Si substrates exhibit a high pore density ($\sim 10^{10}$ pores/cm^2) which can be filled electrochemically to produce multilayered NWs, each NW consisting N SVs connected in series with $N \sim 1-10$.

2. Experimental Methods

2.1. *Fabrication of supported nanoporous anodized aluminum oxide templates*

The process starts with a Physical Vapor Deposition (PVD: e-beam or sputtering) of a conducting underlayer on a carefully cleaned substrate, like Si, SiO_2, sapphire, glass, etc. This conducting layer has a double role, first to serve as anodization barrier during anodization of Al layer deposited on it and then to be a contact electrode both during anodization and further electrochemical growth of NWs inside the pores of the AAO. This conducting layer should also not oxidize under electrochemical conditions usually being a layer of Au or Pt. Intermediate adherence layers (i.e., Ti or Cr) are used between the substrate and the conducting layer. The next step is the Al layer deposition [see Fig. 1(a)] which is a critical procedure in the sense that small thicknesses (up to few hundreds nm) are easy to realize but thicker ones need special deposition conditions. The substrate temperature and deposition rate are key factors for obtaining compact Al layers without hillock and pitting defects.[40] When substrate temperature is kept constant at about 300 K for deposition rates larger than 300 Å/min., e-beam deposited Al layers are compact and

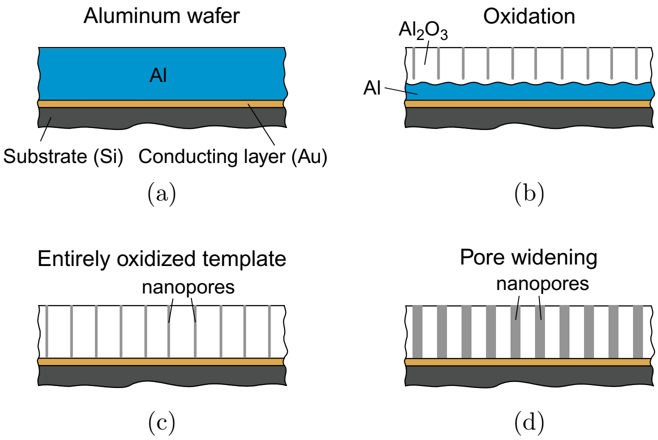

Fig. 1. (a)–(d) Schematic representation of the various steps for the fabrication of the supported nanoporous alumina templates. Adapted from Ref. 42.

without defects. The deposit is polycrystalline with grain sizes (and surface roughness) decreasing with increasing the deposition rate. Experimental investigations showed that high rates (up to 6000 Å/min. at room temperature) allowed the realization of e-beam deposited Al layers with thicknesses up to 10 μm. On the other hand, using sputtering deposition, the Al thickness could reach up to 2 μm for deposition rates of ~1000 Å/min. and at low substrate temperatures (around 5–7°C).[41] The Al adherence is also crucial, since during alumina processing, a strong internal stress is involved. Soft plasma etching (PE) surface treatments coupled with the use of thin Ti intermediate layers are carried out. Ti is particularly preferred, since it acts also as an oxidation brake during the anodization process.

The anodization at constant voltages of the supported Al layer is then performed in similar conditions as for the case of classical Al foils anodization using sulfuric, oxalic or phosphoric acid solutions. In order to decrease the reaction speed of the oxidation and for a better control over thin layers anodization, a low working temperature of about 0°C is used. By limiting the current at the end of the process, when no more metallic Al remains on the substrate, a nearly defect free structure with nanopores down to the conducting underlayer is obtained [see Figs. 1(b) and 1(c)]. A subsequent pore enlargement step eliminates the remaining barrier oxide layer at the bottom of the pores and tunes the pore diameters correspondingly [see Fig. 1(d)]. The widening process is a chemical attack using mainly sulfuric or phosphoric acid solutions at temperatures ranging between 30°C and 40°C. The obtained template is well suited for the growth of NWs inside its nanopores by using electrochemical routes (see Sec. 2.2). By using adequate substrates and underlayers, the entire assembly resists to high temperatures of more than 1000°C allowing further thermal treatments. By controlling the preparation conditions, the geometrical properties of the entire template can be easily controlled. When using thicker Al layers, a two-step anodization can be performed in applications requiring a highly-ordered arrangement of the nanopores.[42]

In our particular case, the sample fabrication process begins with the anodization of about 1 μm thick Al layer sputtered onto a Si/Nb(30 nm)/Au (50 nm)/Ti(6 nm) substrate. The nanopores in the template are formed by complete anodic oxidation of the Al layer in 0.3 M oxalic acid solution at 2°C under a constant voltage of 60 V, followed by a chemical widening process of the pores in a 0.5 M H_2SO_4 solution for about 2 h at 40°C. The pore length and pore diameter at the bottom region are about 1.35 μm and 100 nm, respectively.

2.2. *Electrodeposition of arrays of Co/Cu/Co nanowire spin-valves*

The NW array fabrication process begins with an empty supported alumina nanoporous membrane as illustrated in Fig. 2(a) (see Sec. 2.1). The Au layer at the bottom of the pores serves as a working electrode for subsequent electrodeposition. The final thickness of the alumina template is about 1.3 μm, and the pore density can be as high as 5×10^9 cm^{-2}.

Electrodeposition into the pores is carried out in a conventional three-electrode cell with a platinum (Pt) counter electrode and a Ag/AgCl reference electrode [see Fig. 2(b)]. An array of NWs each containing a stack of several in series connected pseudo SVs Co(7 nm)/Cu(13 nm)/Co(24 nm) [see Fig. 2(c)] is then electrochemically synthesized in a single bath using a pulse potential deposition technique,[23,27,38,39,43] i.e., by switching between the deposition potentials of the two constituents (−0.5 V and −0.95 V for Cu and Co deposition, respectively).

The composition of the aqueous electrolytic solution is as follows: $CoSO_4 \cdot 7H_2O$ (1M), $CuSO_4 \cdot 5H_2O$

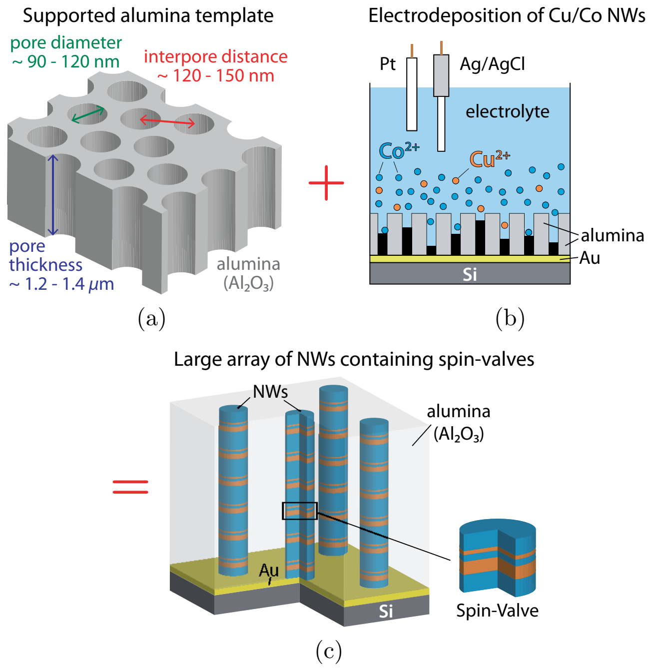

Fig. 2. (a) Empty nanoporous alumina template. (b) Schematic of the electrochemical cell for the electrodeposition of Cu/Co nanowires. (c) Schematic of the resulting array of SV nanowires.

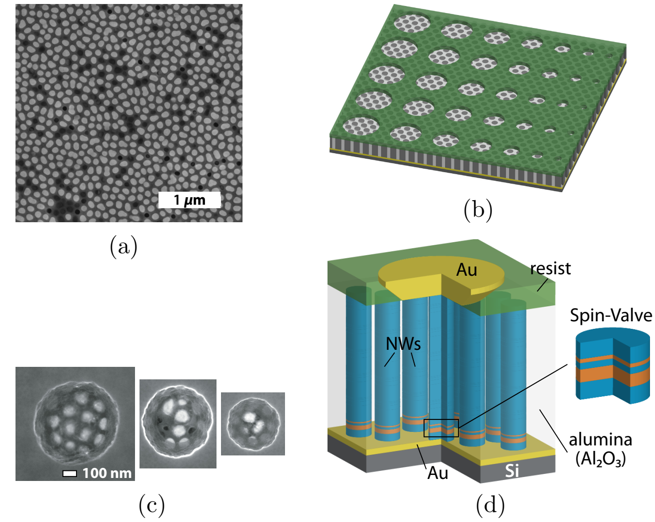

Fig. 3. (a) Top view scanning electron microscopy (SEM) image of the SV nanowire array embedded in the AAO template. (b) Schematic showing a resist pattern from an assembly of circular apertures of different sizes. (c) SEM images for three different openings showing the extremities of the nanowires at the surface of the template. (d) Illustration of the completely structured device with single SVs located at the bottom of each NW.

(15 mM) and H_3BO_3 (0.5 M). Then, the pores are filled electrochemically with Cu. Each SV is separated from the former by a 100 nm thick Cu spacer layer. Then, the pores are filled electrochemically with Cu and the filled template is thinned by mechanical polishing. The latter can have a resolution of a few tens of nm using colloidal silica (Syton®) and is performed to expose most of the nanowire extremities at the surface of the AAO template [see Fig. 3(a)].

At the end of the electrodeposition and after the mechanical polishing of the filled AAO templates, a high density of NWs end up at the template surface as seen in Fig. 3(a).

2.3. *Nanoscale electrical contacts made using e-beam lithography*

In a recent work,[27] the use of electron beam lithography (EBL) for parallel connection of a limited number of SV nanowires (typically less than 5) was demonstrated.

Once a high density of NWs slightly emerges from the AAO pore openings [see Fig. 3(a) and schematic illustration in Fig. 4(a)], the next step consists in covering the entire surface of the filled AAO template with a 300 nm thick silicon nitride (Si_3N_4) mask deposited by plasma enhanced chemical vapor deposition (PECVD) at low temperature $T = 150°C$ [see Fig. 4(b)]. A 200 nm thick polymethyl methacrylate (PMMA) layer is then spin-coated from

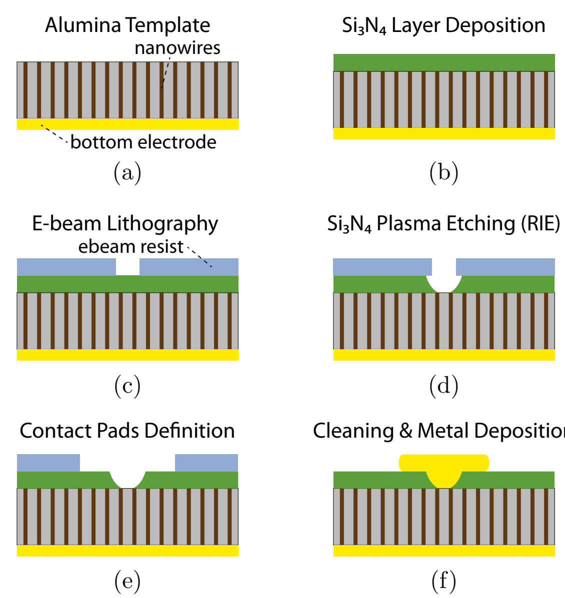

Fig. 4. Schematic illustration of the EBL-based electrical contacting technique.

a diluted solution 4% in anisole (Microchemicals GmbH) and baked in an oven at 150°C for 5 min. The electron beam exposure was done at 30 keV with an intensity of few tens of pA. The exposed pattern is developed in a mixture of methyl-isobutyl-ketone/isopropanol (IPA), rinsed in IPA and de-ionized water, and then blow dried with nitrogen [see Fig. 4(c)]. The pattern realized in PMMA is then transferred to the Si_3N_4 mask by reactive ion etching [RIE, see Fig. 4(d)]. By adjusting the exposure dose [see Figs. 3(b), 3(c) and 4(e)], a resolution better than 40 nm is achieved. Finally, electrical contact with the nanowires is made with 150 μm wide Au pads defined by EBL followed by Ti/Au metalization [see Figs. 3(d) and 4(f)]. By this method, we were able to contact a single wire from a dense NW forest.

2.4. *Set-up for the measurement of STT driven microwave emission*

Our experimental set-up is schematically shown in Fig. 5. The sample is placed inside an electromagnet capable of applying static magnetic fields up to $H =$ 9 kOe and thus also able to sweep the magnetic field from -9 to $+9$ kOe. A DC current I_{DC} delivered by a DC current source flows through the sample and a nanovoltmeter records the subsequent voltage for magneto-transport measurements purposes. A bias-T is placed in between the DC circuit and the sample, so that the AC signal produced by the sample can be captured, amplified by a Low Noise Amplifier (LNA) and recorded by a high performance spectrum analyzer.

A data acquisition system for measuring GMR signal and microwave emission was developed using LabView®. First, magneto-transport measurements are performed using a small DC current. Then, a higher density of current is injected into the nanowire, optionally in the presence of an external magnetic field for exploring combined GMR and STT effects responsible for microwave emission as discussed in the next section. The current used for the measurements was limited to 6.0 mA to prevent from heating due to Joule effect, so that current densities as large as $\sim 6 \times 10^7$ A/cm^2 were injected on a single NW without deterioration.

The acquisition of microwave signals is performed using a spectrum analyzer after amplification (30–40 dBm). For that purpose, a high performance spectrum analyzer measuring signals up to a frequency of 7.5 GHz was used.

When the conditions are fulfilled, the GMR signal owing to the STT excitation of the magnetization of the sample is materialized by an microwave emission peak on the spectrum analyzer.

2.5. *Micromagnetic simulation method of the nanowire spin-valves*

For the micromagnetic simulations, a circular metallic SV nanopillar of 80 nm in diameter is considered. The studied SV consists of a Co (7 nm)/Cu(13 nm)/Co(24 nm) stack as shown in Fig. 6. The parameters for the magnetic properties of Co are as follows: $A = 1.3 \times 10^{-6}$ erg/cm, $\alpha_G = 0.011$,[44] $M_s = 1200$ emu/cm^3,[45] where A, α_G and M_s are respectively, the exchange stiffness constant, the Gilbert damping parameter and the saturation magnetization. The smaller value of M_s compared to $M_s = 1422$ emu/cm^3 for pure Co as well as the absence of magneto-crystalline

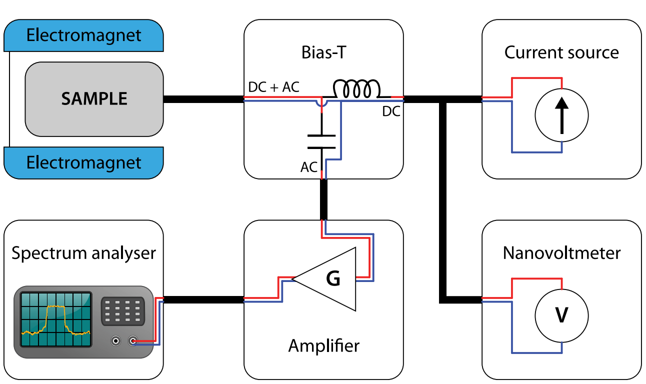

Fig. 5. Schematic illustration of the set-up used for the magneto-transport and microwave emission measurements.

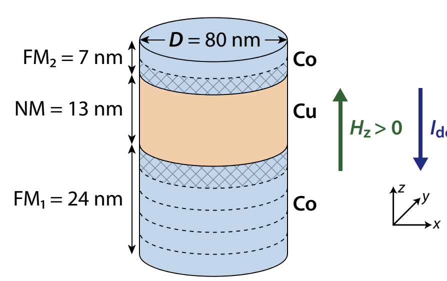

Fig. 6. Sketch of the SV stack used in the micromagnetic simulations ($FM_1 = FM_2 =$ cobalt; NM = copper). The thick magnetic layer (FM_1) is divided into five 4.8 nm thick sub-layers and the thin magnetic layer is divided into two 3.5 nm thick sub-layers. Spin torque acts only on the hatched sublayers. The applied external magnetic field orientation and the convention direction of positive current are also shown.

anisotropy[39] are chosen to reproduce the experimental parameters known for electrodeposited nanowires. Indeed, as both ions of Co and Cu are present in the electrolyte solution the Co layers contain atoms of Cu thus giving rise to a reduction of the M_s value and to the suppression of the magneto-crystalline anisotropy.

The step of the computational mesh is $2\,\mathrm{nm} \times 2\,\mathrm{nm}$ in the plane and 3.5 nm (resp. 4.8 nm) in the perpendicular direction for the thin (resp. thick) magnetic layer. The in-plane dimensions were taken to be below the exchange length $L_{ex} = \sqrt{A/(2\pi M_s^2)} = 3.8\,\mathrm{nm}$ to ensure proper behavior between two adjacent discretization cells of the SV system with respect to the exchange interaction.

In a CPP-GMR SV, the electrons of an injected DC current acquire spin polarization (due to relaxation and spin accumulation), either by passing through a so-called polarizer layer or by being reflected from the latter. As shown hereafter and unlike most of the micromagnetic simulations made till now on such type of SVs, the magnetization of the polarizer layer is not kept fixed. The consequence is that both magnetic layers in the SV stack can act simultaneously as a polarizer and as a free layer.

The aim of the micromagnetic calculations made for the SV depicted in Fig. 6 is to identify both magnetic ground states and magnetization dynamics of the two magnetic layers (FM_1 and FM_2) that made up the SV. The resulting information is studied as a function of the injected current and for different magnetic field intensities applied along the rod axis of the SV.

The dynamics of the magnetization is investigated using the micromagnetic solver SpinPM®.[a] In this code, the magnetization is resolved by numerical integration of the Landau–Lifshitz–Gilbert (LLG) equation taking into account the spin-transfer-torque effect.[5,46] The LLG equation with STT is written as follows:

$$\frac{\partial \mathbf{M}}{\partial t} = -\gamma \mathbf{M} \times \mathbf{H}_{\mathrm{eff}} + \frac{\alpha_G}{M_s} \mathbf{M} \times \frac{\partial \mathbf{M}}{\partial t} + \mathbf{\Gamma}_{\mathrm{STT}}, \quad (1)$$

where $\gamma = \mu_0 \gamma_e$ is the Gilbert gyromagnetic ratio with $\gamma_e = g_e \mu_B/\hbar$, the electron gyromagnetic ratio ($\gamma \cong 1.76 \times 10^7$ (Oe·s)$^{-1}$ in CGS units, g_e is the electron g-factor, μ_B is the Bohr magneton, $\hbar$ is the reduced Plank constant) and $\mathbf{H}_{\mathrm{eff}}$ is the effective field. The latter is the sum of the magnetostatic field, the exchange field, the Oersted field, and the anisotropy field. $\mathbf{\Gamma}_{\mathrm{STT}}$ is the spin-transfer torque contribution to the LLG equation. It originates from the spin transfer effect between the polarized electrons from the injected dc current and the electrons responsible for the magnetization in a free magnetic layer. $\mathbf{\Gamma}_{\mathrm{STT}}$ is divided into two components, i.e., $\mathbf{\Gamma}_{\mathrm{STT}} = \mathbf{\Gamma}_{\mathrm{CPP}} + \mathbf{\Gamma}_{\mathrm{FLT}}$. $\mathbf{\Gamma}_{\mathrm{CPP}}$ refers to the Slonczewski torque and Γ_{FLT} refers to the field-like torque. Knowing that in our CPP-SV the current flows perpendicularly to the layer's plane, the $\mathbf{\Gamma}_{\mathrm{FLT}}$ term is neglected[47,48] (in metallic spin-valves, CPP geometry, $\mathbf{\Gamma}_{\mathrm{FLT}}$ is typically less than 5% of $\mathbf{\Gamma}_{\mathrm{CPP}}$) and the $\mathbf{\Gamma}_{\mathrm{CPP}}$ torque is given by

$$\mathbf{\Gamma}_{\mathrm{CPP}} = -a_J \frac{\gamma}{M_s} \mathbf{M} \times (\mathbf{M} \times \mathbf{m}_{\mathrm{ref}}), \quad (2)$$

where M_s is the saturation magnetization, $\mathbf{m}_{\mathrm{ref}}$ is unit vector along the magnetization direction of the polarizing magnetic layer (the reference layer responsible for the polarized current), and a_J is the STT amplitude term:

$$a_J = P \frac{\hbar}{2|e|} \frac{J}{M_s d}, \quad (3)$$

where P is the current polarization, J is the current density, $|e|$ is the charge of the electron, and d is the free magnetic layer thickness.

Before choosing the cell size for the simulations, different tests were performed using vertical and horizontal cell dimensions much smaller than L_{ex}. The in-plane (x-y) cell dimensions were kept much smaller than L_{ex} ($2\,\mathrm{nm} \times 2\,\mathrm{nm}$) for two reasons. First, to properly capture the spin-texture of the vortex cores and second to promote our vortex-core-center-tracker algorithm to achieve better resolution on the vortex core position used for further oscillation frequency evaluation. However, the vertical dimension of the cells has been increased to enhance the rate of calculations. As will be shown later on, an important result of our study is that magnetic vortex ground state is always found in the thick layer (FM_1). As the vertical vortex texture is not modified even in the dynamical regime, we chose to subdivide the 24 nm thick layer into five 4.8 nm thick sub-layers (slightly larger than L_{ex}). In contrast, since the

[a]SpinPM is a micromagnetic code developed by the Istituto P. M. srl (Torino, Italy — www.istituto-pm.it) based on a forth order Runge-Kutta numerical scheme with an adaptative time-step control for the time integration.

ground state in the FM_2 layer is not always the vortex configuration, we preferred to keep the sub-layers smaller than L_{ex} with a thickness of 3.5 nm.

As shown in Fig. 6, only the magnetic sub-layers in contact with the nonmagnetic spacer (hatched sub-layers) are relevant for the STT phenomenon. These sub-layers act as time varying polarizers and feel the polarized current from each other. As a consequence, only a reduced thickness d in Eq. (3) is considered for each magnetic layer, 3.5 nm and 4.8 nm for FM_2 and FM_1 respectively. This artificially increases the spin-torque effect acting on the two layers while ensuring the asymmetry of the STT effect between them.

3. Results

3.1. *Micromagnetic simulations*

In the micromagnetic simulations, a bias magnetic field (H_z) and a dc current (I_{DC}) are applied simultaneously in the out-of-plane direction. The spin torque efficiency is enclosed in the polarization parameter P with a typical value of 0.3. In our convention, the current is positive when the electrons flow from the thick magnetic layer (FM_1) to the thin magnetic layer (FM_2). The calculations start with magnetizations $\mathbf{m} = (1, 1, 0)$ in FM_2 and $\mathbf{m} = (-1, -1, 0)$ in FM_1, and the magnetization then relax to its equilibrium state. The obtained configuration is identified as the most stable one associated with the (I_{DC}, H_z) couple. The same calculations are made for different combinations of H_z and I_{DC} (for I_{DC} from -7 mA to 8 mA every 0.5 mA and for H_z from 0 kOe to 5 kOe for every 0.5 kOe), and the equilibrium states are summarized in the phase diagram shown in Fig. 7.

For any (H_z, I) combination, a magnetic vortex state appears in the thick magnetic layer (FM_1), thus confirming the stability of the vortex state in that thick FM layer. In contrast, for the thin magnetic layer (FM_2), a vortex state, a quasi-uniform state, or a C-like[b] state, is obtained. Figure 7 splits into two distinct regions as far as the ground magnetic state is concerned. The first one refers to the one-vortex states (U/V↑ and C/V↑) and the second one to the two-vortex states (V↑/V↑, V↑/V↓ and V↓/V↑).

The asymmetric response for positive and negative injected currents (see Fig. 7) is due to the fact that FM_1 is thicker than FM_2 and thus constitutes a better polarizer. So for a positive (resp. negative) current, i.e., when electrons flow from FM_1 to FM_2 (resp. from FM_2 to FM_1), the STT effect tends to align (resp. anti-align) the magnetic moments.

The STVOs in Phase B_1 require larger threshold currents than the C-like/V↑ states of Phase A but have the remarkable property of exhibiting sustained oscillation even without any bias magnetic field H_z. The latter feature refers to the particular

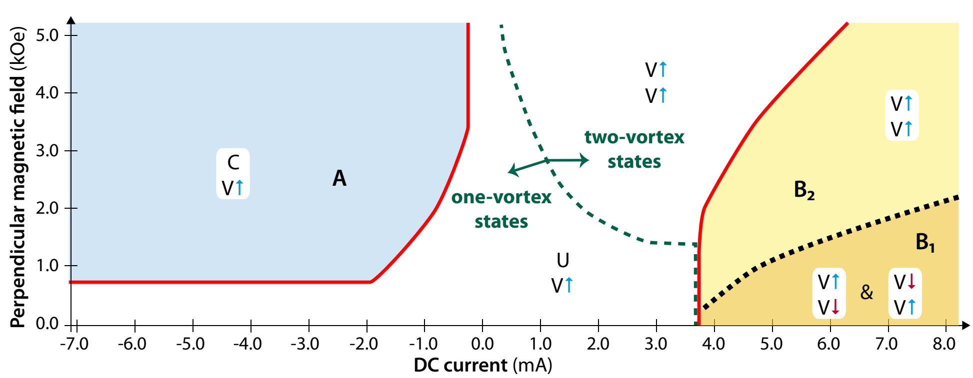

Fig. 7. Phase diagram of the sustained vortex core oscillations driven by the STT effect obtained by micromagnetic simulations. For negative currents, Phase A (blue) refers to one vortex in FM_1 and to a C-like state in FM_2. For positive currents, Phase B refers to two vortices, one in each magnetic layer with the same chirality and with opposite polarities (Phase B_1, dark yellow) or with the same polarity (Phase B_2, yellow). In the other regions, the vortex core oscillations are not maintained steadily. The notations are as follows: U = quasi-uniform magnetic state, C = C-like quasi-uniform magnetic state, V↑ = vortex with up polarity, and V↓ = vortex with down polarity (color online).

[b]The C-like state is a quasi-uniform state with a small variation of successive momenta in the whole volume in such a way to show a C (or banana) curvature in the magnetization distribution.

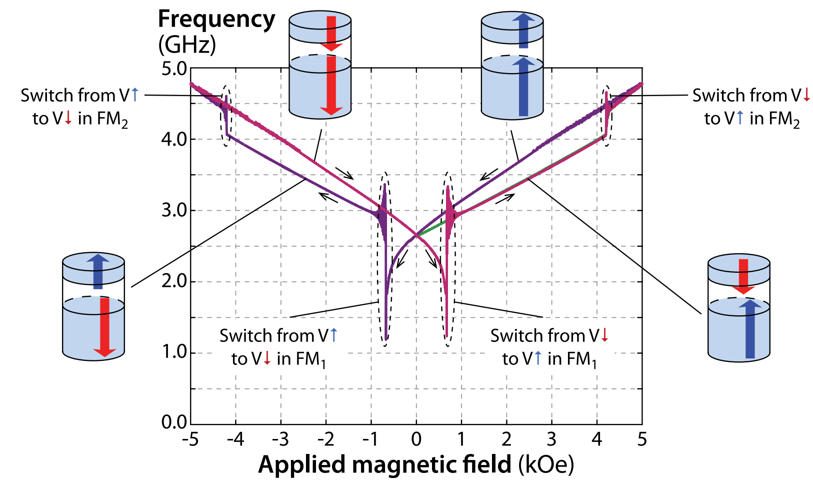

Fig. 8. Magnetic field dependence of the vortex oscillation frequency for a full sweep in field starting from 0 kOe to ±5 kOe and a positive injected dc current of 6 mA (Phases B_1 and B_2 STVOs in Fig. 7).

case where the vortex polarities of the two FM layers are opposite as also reported by Locatelli *et al.*[22]

Phase B in Fig. 7 refers to the steady oscillating two-vortex state configurations such as V↑/V↑, V↑/V↓, V↓/V↑, and V↓/V↓. The configuration V↓/V↓ is not shown in phase diagram of Fig. 7 as it requires a negatively applied magnetic field. Nevertheless, as will be shown in the following study, if the V↓/V↓ configuration is first stabilized, it is still stable for a weak positive magnetic field. The two-vortex state oscillates in a sustained mode driven by spin-transfer once the injected positive current reaches a critical current value, depending on the H_z value.

Furthermore, the different magnetic configurations of Phase B can be reached by applying magnetic field for a full cycle to the two-vortex state. To illustrate this, starting from Phase B_1 STVO configuration V↓/V↑ for $I_{DC} = 6$ mA and at zero magnetic field, successive linear magnetic field ramps are applied as follows: from 0 kOe to 5 kOe, then from 5 kOe to −5 kOe, and finally from −5 kOe to 5 kOe. The resulting frequency versus field feature is reported in Fig. 8.

In Fig. 8, one can see the different switch in polarity between states V↑ and V↓ for the two FM layers of the STVO (at ±4.2 kOe for FM_2 and at ±0.7 kOe for FM_1). The switch is marked by an abrupt jump in the frequency feature and this jump is larger when the switch refers to FM_1. Another remarkable property exhibited by Fig. 8 is that the thick magnetic layer drives the dynamics as the slope of the frequency versus magnetic field characteristics is dictated by the thick layer vortex polarity.

Considering the states V↓/V↑ and V↑/V↓ shown in Phase B_1, it is possible to obtain the complete frequency versus magnetic field curves (see Fig. 9). Indeed, starting from a magnetic field of about 4 kOe (i.e., a field just below the switching field of the FM_2 vortex polarity) and thus considering the V↓/V↑ magnetic state, a decreasing magnetic field sweep is applied to the STVO. The field sweep is stopped as soon as the switching field of FM_1 vortex polarity is reached (at about −3.8 kOe). A similar magnetic field sweep is applied to the magnetic state V↑/V↓ starting from about −4 kOe up to 3.8 kOe (which corresponds to the switching field of the FM_1 vortex polarity).

As shown in Fig. 9, the two curves (the blue one with positive slope for state V↓/V↑ and the red one

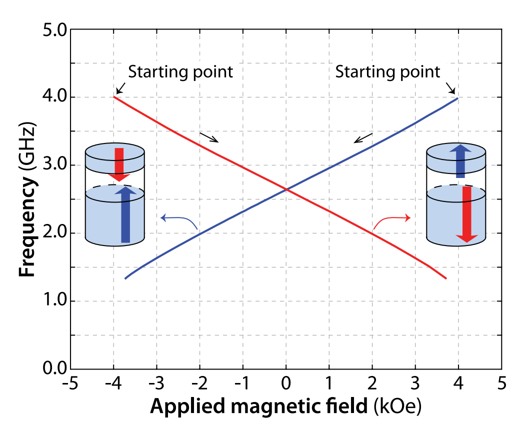

Fig. 9. Evolution of the vortex core frequency as a function of the applied magnetic field (along z-axis) for a positive injected dc current of 6 mA (Phase B_1 STVOs in Fig. 7).

with negative slope for state V↑/V↓) are symmetric and cross each other at zero bias magnetic field. Furthermore, the oscillating frequency versus magnetic field features obtained are linear and their slopes are directly related to the vortex polarity of the thick magnetic layer that composes the STVO.

3.2. *Microwave emission from single nanowire spin-torque oscillator*

As detailed in Sec. 3.1, micromagnetic simulations were performed to predict and characterize the ground magnetic states of metallic SVs. Furthermore, simulations also offer the opportunity to identify the current and magnetic field conditions for the observations of steady state oscillations. As shown hereafter, microwave signals have been observed experimentally on single Co/Cu/Co nanowire SVs even at zero magnetic field. Interestingly, high frequency versus magnetic field tunability was demonstrated, in the range 0.4–2 MHz/Oe, depending on the orientation of the applied magnetic field relative to the magnetic layers of the pseudo spin-valve. However, it is stressed that the individual layer thicknesses and wire diameter in the simulations (24/13/7 nm thickness for the spin-valves and 80 nm wire diameter) differ slightly from the experimental STVOs (22/12/6 nm thickness and 100 nm diameter). The difficulties in controlling precisely the individual layer thicknesses and wire diameter while fabricating the porous alumina template and electrodeposited spin-valve nanowires are responsible for these differences. However, despite these small disagreement, the frequency values and the variation of the emitted signal as a function of the external magnetic field are in good agreement with micromagnetic simulations.

Electric transport measurements were then performed to characterize the resistance and magnetic configuration of the single NW. Magnetoresistance curves obtained for a positive current of 4.0 mA are shown in Fig. 10. The single NW resistance is about 18 Ω. The GMR value is $\Delta R = 21\,\mathrm{m}\Omega$ while sweeping the in-plane applied magnetic field and $\Delta R = 12$ mΩ in out of plane field (see inset of Fig. 10). These results indicate that an anti-parallel magnetization configuration can be more easily obtained when the field is oriented in the plane of the layers. Also, as expected, the easy axis of the nanomagnet was set by the shape anisotropy to be perpendicular to the wire axis, i.e., in the plane of the layers.

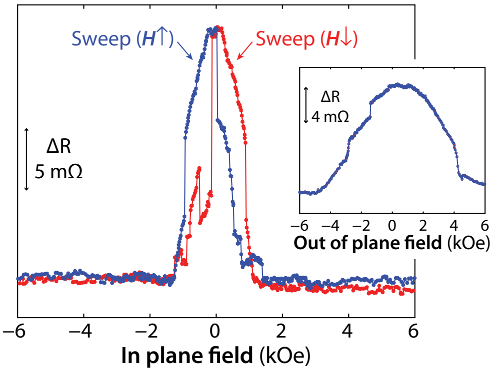

Fig. 10. GMR curves measured by contacting a single NW (made of a single Co(22 nm)/Cu(12 nm)/Co(6 nm) SV) with the magnetic field applied in the plane of the layers (IP field). The inset shows the GMR curve obtained by sweeping the external field along the wire axis (out of plane (OOP) field).

Microwave emission measurements are performed with a spectrum analyzer after a 42-dBm amplification of the output oscillating GMR signal. Selected experimental results of spin-transfer-driven vortex excitation obtained by measuring a single SV are displayed in Fig. 11.

To stabilize the magnetic vortex state, a saturating perpendicular magnetic field is first applied to

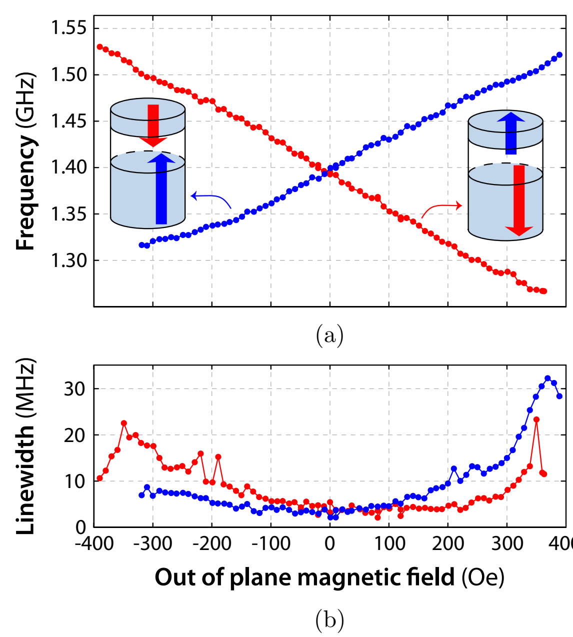

Fig. 11. (a) Evolution of the emitted signal frequency as a function of the perpendicular applied magnetic field for the two magnetization configurations V↓/V↑ (in blue) and V↑/V↓ (in red). The signal was obtained by injecting a positive dc current of 6.0 mA. (b) The linewidth versus magnetic field for both magnetization configurations in the corresponding colors [Corresponds to Phase B_1 in Fig. 7] (color online).

the sample before a decreasing ramp of magnetic field. Experimental evidence for the presence of vortex states in the Co layers has been demonstrated by Wong *et al.*[49] on the same type of electrodeposited multilayered NWs.

The results reported for the measured STVO are related to the two-vortex state with vortices of opposite polarity present in both the magnetic layers of the SV. The two possible magnetic configurations are V↑/V↓ and V↓/V↑. V↑/V↓ (resp. V↓/V↑) refers to a vortex with up (resp. down) polarity in the thin magnetic layer and a vortex with down (resp. up) polarity in the thick magnetic layer. The magnetic states responsible for the microwave emission are also consistent with micromagnetic simulations.[23]

By applying a perpendicular magnetic field and passing a dc current through the single SV, narrow peaks are observed in the recorded emission spectra. Figure 11(a) displays the frequency versus magnetic field features for a positive injected dc current of 6.0 mA. The current is defined as positive when the electrons flow from the thick magnetic layer to the thin magnetic layer in the Co(22 nm)/Cu(12 nm)/Co(6 nm) SV.

The sign of the slope of the frequency-field features [see Fig. 11(a)] is directly related to the relative alignment between the polarity of the vortex in the thick magnetic layer of the SV and the magnetic field direction. The experimental data are consistent with the remarkable properties of the magnetic configurations V↑/V↓ and V↓/V↑ as reported by Ref. 22, and as shown by our micromagnetic simulations (see Fig. 9). Indeed, when comparing the data shown in Figs. 9 and 11(a) and despite a zero field frequency shift of about 1 GHz between experiment and simulations, there is a satisfactory overall agreement.

Thanks to the two-vortex states with opposite polarity, the microwave emission appears even without any bias magnetic field and the frequency-field characteristics are linear. The slopes of the curves are similar to the ones obtained using micromagnetic simulations (see Fig. 9), about 0.37 GHz/kOe. As shown in Fig. 11(b), signal quality improvement is also obtained at zero field, i.e., the linewidth decreases. In contrast, when using a lithographically defined nanopillar SV, the minimum of the linewidth is shifted and is obtained at a relatively large magnetic field,[22] around 600 Oe.

Moreover, the relatively low linewidth observed in all the emission spectra is consistent with the vortex gyrotropic motion. Indeed, the measured linewidth was as low as 1.8 MHz for a positive dc current of 6.0 mA. The maximum power obtained is about 99 fW/mA^2. The results also corroborate the nucleation of a two-vortex state for positive currents as obtained in the micromagnetic study[23] thus giving rise to a better spectral quality of the signal (i.e., lower linewidth and larger peak height).

Another remarkable property of our electrodeposited STVO is the large field-frequency tunability. It approximates 0.4 MHz/Oe for an out of plane field sweep, but is even larger and reaches 2 MHz/Oe for an in plane field sweep.[27]

4. Conclusion

As far as applications of STVOs is concerned, that kind of STVOs based on the spin transfer driven dynamics of two coupled vortices in template grown spin-valve nanopillars are very promising. Indeed, the microwave signals originating from the combined SST and GMR effects can be obtained without any static bias magnetic field when the two-vortex states with opposite polarity are used. In addition, the vortex-based nano-oscillators exhibit improved spectral quality compared to nonvortex ones. Furthermore, the electron beam lithography is a versatile tool capable of connecting a single or a desired number of spin-torque vortex oscillators from the dense forest-like structure of nanowires embedded in nanoporous AAO templates integrated onto Si wafers with better compatibility to the standard CMOS processes.

Acknowledgments

The authors would like to kindly acknowledge V. Antohe, L. Gence, M. Darques, V. Cros, and A. Khvalkovskiy for their contributions and technical help. This work was partly supported by the Fédération Wallonie-Bruxelles (ARC 13/18-052, Supracryst) and by the Fonds de la Recherche Scientifique — FNRS under Grant No. T.0006.16.

References

1. M. D. Stiles and J. Miltat, Spin-transfer torque and dynamics, in *Spin Dynamics in Confined Magnetic Structures III*, eds. B. Hillebrands and A. Thiaville (Springer, Berlin Heidelberg, 2006), pp. 225–308.
2. J. Katine and E. E. Fullerton, *J. Magn. Magn. Mater.* **320**, 1217 (2008).

3. T. J. Silva and W. H. Rippard, *J. Magn. Magn. Mater.* **320**, 1260 (2008).
4. D. Berkov and J. Miltat, *J. Magn. Magn. Mater.* **320**, 1238 (2008).
5. J. C. Slonczewski, *J. Magn. Magn. Mater.* **159**, L1 (1996).
6. L. Berger, *Phys. Rev. B.* **54**, 9353 (1996).
7. J.-V. Kim, V. S. Tiberkevich and A. N. Slavin, *Phys. Rev. Lett.* **100**, 017207 (2008).
8. M. W. Keller, M. R. Pufall, W. H. Rippard and T. J. Silva, *Phys. Rev. B.* **82**, 054416 (2010).
9. A. N. Slavin and V. S. Tiberkevich, *IEEE Trans. Magn.* **45**, 1875 (2009).
10. S. Y. Martin, C. Thirion, C. Hoarau, C. Baraduc and B. Diény, *Phys. Rev. B.* **88**, 024421 (2013).
11. E. Iacocca and J. Åkerman, *Phys. Rev. B.* **85**, 184420 (2012).
12. B. Georges, J. Grollier, M. Darques, V. Cros, C. Deranlot, B. Marcilhac, G. Faini and A. Fert, *Phys. Rev. Lett.* **101**, 017201 (2008).
13. V. E. Demidov *et al.*, *Nat. Commun.* **5**, 3179 (2014). DOI: 10.1038/ncomms4179.
14. M. R. Pufall, W. H. Rippard, M. L. Schneider and S. E. Russek, *Phys. Rev. B.* **75**, 140404 (2007).
15. V. S. Pribiag, I. N. Krivorotov, G. D. Fuchs, P. M. Braganca, O. Ozatay, J. C. Sankey, D. C. Ralph and R. A. Buhrman, *Nat. Phys.* **3**, 498 (2007).
16. Q. Mistral, M. van Kampen, G. Hrkac, J.-V. Kim, T. Devolder, P. Crozat, C. Chappert, L. Lagae and T. Schrefl, *Phys. Rev. Lett.* **100**, 257201 (2008).
17. A. Ruotolo, V. Cros, B. Georges, A. Dussaux, J. Grollier, C. Deranlot, R. Guillemet, K. Bouzehouane, S. Fusil and A. Fert, *Nat. Nano.* **4**, 528 (2009).
18. M. Manfrini, T. Devolder, J.-V. Kim, P. Crozat, N. Zerounian, C. Chappert, W. Van Roy, L. Lagae, G. Hrkac and T. Schrefl, *Appl. Phys. Lett.* **95**, 192507 (2009).
19. R. Lehndorff, D. Burgler, C. Schneider and Z. Celinski, *Appl. Phys. Lett.* **97**, 142503 (2010).
20. A. Dussaux, A. Khvalkovskiy, J. Grollier, V. Cros, A. Fukushima, M. Konoto, H. Kubota, K. Yakushiji, S. Yuasa, K. Ando and A. Fert, *Appl. Phys. Lett.* **98**, 132506 (2011).
21. X. W. Yu, V. S. Pribiag, Y. Acremann, A. A. Tulapurkar, T. Tyliszczak, K. W. Chou, B. Bräuer, Z.-P. Li, O. J. Lee, P. G. Gowtham, D. C. Ralph, R. A. Buhrman and J. Stöhr, *Phys. Rev. Lett.* **106**, 167202 (2011).
22. N. Locatelli, V. V. Naletov, J. Grollier, G. De Loubens, V. Cros, C. Deranlot, C. Ulysse, G. Faini, O. Klein and A. Fert, *Appl. Phys. Lett.* **98**, 062501 (2011).
23. F. Abreu Araujo, M. Darques, K. A. Zvezdin, A. V. Khvalkovskiy, N. Locatelli, K. Bouzehouane, V. Cros and L. Piraux, *Phys. Rev. B.* **86**, 064424 (2012).
24. A. D. Belanovsky, N. Locatelli, P. N. Skirdkov, F. Abreu Araujo, J. Grollier, K. A. Zvezdin, V. Cros and A. K. Zvezdin, *Phys. Rev. B.* **85**, 100409(R) (2012).
25. N. Locatelli, A. Ekomasov, A. Khvalkovskiy, S. Azamatov, K. Zvezdin, J. Grollier, E. Ekomasov and V. Cros, *Appl. Phys. Lett.* **102**, 062401 (2013).
26. A. D. Belanovsky, N. Locatelli, P. N. Skirdkov, F. Abreu Araujo, K. A. Zvezdin, J. Grollier, V. Cros and A. K. Zvezdin, *Appl. Phys. Lett.* **103**, 122405 (2013).
27. F. Abreu Araujo, L. Piraux, V. A. Antohe, V. Cros and L. Gence, *Appl. Phys. Lett.* **102**, 222402 (2013).
28. R. Lebrun, N. Locatelli, S. Tsunegi, J. Grollier, V. Cros, F. Abreu Araujo, H. Kubota, K. Yakushiji, A. Fukushima and S. Yuasa, *Phys. Rev. Appl.* **2**, 061001 (2014).
29. N. Locatelli, V. Cros and J. Grollier, *Nat. Mater.* **13**, 11 (2014).
30. N. Locatelli, A. Mizrahi, A. Accioly, D. Querlioz, J.-V. Kim, V. Cros and J. Grollier, Spin torque nanodevices for bio-inspired computing, in *2014 14th Int. Workshop Cellular Nanoscale Networks and their Applications (CNNA)*, 7, 2014. DOI: 10.1109/CNNA.2014.6888659.
31. A. Dussaux, B. Georges, J. Grollier, V. Cros, A. Khvalkovskiy, A. Fukushima, M. Konoto, H. Kubota, K. Yakushiji, S. Yuasa, K. Zvezdin, K. Ando and A. Fert, *Nat. Commun.* **1**, 8 (2010).
32. B. Georges, J. Grollier, V. Cros and A. Fert, *Appl. Phys. Lett.* **92**, 232504 (2008).
33. S. Kaka, M. R. Pufall, W. H. Rippard, T. J. Silva, S. E. Russek and J. A. Katine, *Nature* **437**, 389 (2005).
34. E. Iacocca and J. Åkerman, *J. Appl. Phys.* **110**, 103910 (2011).
35. J. Grollier, V. Cros and A. Fert, *Phys. Rev. B.* **73**, 060409 (2006).
36. Y. Zhou and J. Åkerman, *Appl. Phys. Lett.* **94**, 112503 (2009).
37. H. Chen, J. Chang and C. Chang, *SPIN* **01**, 1 (2011).
38. L. Piraux, K. Renard, R. Guillemet, S. Mátéfi-Tempfli, M. Mátéfi-Tempfli, V. A. Antohe, S. Fusil, K. Bouzehouane and V. Cros, *Nano Lett.* **7**, 2563 (2007).
39. M. Darques, A.-S. Bogaert, F. Elhoussine, S. Michotte, J. de la Torre Medina, A. Encinas and L. Piraux, *J. Phys. D. Appl. Phys.* **39**, 5025 (2006).
40. L. Mattsson, Y. H. L. Page and F. Ericson, *Thin Solid Films* **198**, 149 (1991).
41. A. Vlad, Advanced Fabrication of Nanowire Arrays and Three-Dimensional Nanostructures, PhD thesis, École Polytechnique de Louvain, Université catholique de Louvain 2009.
42. S. Mátéfi-Tempfli, M. Mátéfi-Tempfli, A. Vlad, V. Antohe and L. Piraux, *J. Mater. Sci., Mater. Electron.* **20**, 249 (2009).

43. S. Dubois, C. Marchal, J. M. Beuken, L. Piraux, J. L. Duvail, A. Fert, J. M. George and J. L. Maurice, *Appl. Phys. Lett.* **70**, 396 (1997).
44. M. Oogane, T. Wakitani, S. Yakata, R. Yilgin, Y. Ando, A. Sakuma and T. Miyazaki, *Jpn. J. Appl. Phys.* **45**, 3889 (2006).
45. M. Darques, A. Dussaux, A. V. Khvalkovskiy, J. De la Torre Medina, F. Abreu Araujo, R. Guillemet, K. Bouzehouane, S. Fusil, J. Grollier, G. G. Avanesyan, K. A. Zvezdin, V. Cros and L. Piraux, *J. Phys. D. Appl. Phys.* **44**, 105003 (2011).
46. A. V. Khvalkovskiy, J. Grollier, A. Dussaux, K. A. Zvezdin and V. Cros, *Phys. Rev. B.* **80**, 140401 (2009).
47. K. Xia, P. J. Kelly, G. E. W. Bauer, A. Brataas and I. Turek, *Phys. Rev. B.* **65**, 220401 (2002).
48. M. D. Stiles and A. Zangwill, *Phys. Rev. B.* **66**, 014407 (2002).
49. J. Wong, P. Greene, R. K. Dumas and K. Liu, *Appl. Phys. Lett.* **94**, 032504 (2009).